# Composite Acoustic Metamaterial for Broadband Low-Frequency Acoustic Attenuation

Ao Chen,[1,2] Zhiwei Yang,[1,2] Xiaoguang Zhao,[2,3] Stephan Anderson,[2,3,†] and Xin Zhang[1,2,*]

[1] *Department of Mechanical Engineering, Boston University, Boston, Massachusetts 02215, USA*
[2] *Photonics Center, Boston University, Boston, Massachusetts 02215, USA*
[3] *Department of Radiology, Boston University Medical Campus, Boston, Massachusetts 02118, USA*

(Received 3 March 2023; revised 11 May 2023; accepted 15 June 2023; published 7 July 2023)

We propose a composite acoustic metamaterial consisting of Mie resonators and a Helmholtz resonator array. Such a design achieves a broadband acoustic attenuation in the low-frequency regime. This wideband soundproofing effect may be explained using the transfer-matrix method and the lumped-element model. Transmission loss and transmittance are robust and tested both numerically as well as experimentally. Through the composite design, using a deep-subwavelength structure, we successfully achieve a broadband low-frequency acoustic attenuation that blocks over 90% of incident acoustic energy within a frequency range of 1250 Hz. Our work offers a design paradigm by which to realize extraordinary airborne acoustic silencing in low-frequency regimes.

DOI: 10.1103/PhysRevApplied.20.014011

## I. INTRODUCTION

Noise attenuation is a longstanding challenge in applied acoustics. Conventionally, acoustic attenuation is realized through acoustic barriers by either reflecting or absorbing incident acoustic energy. While wideband acoustic attenuation may be obtained using such conventional approaches, attenuation in the low-frequency regime ($<$1000 Hz) remains challenging using such methods given the long acoustic wavelength [1]. Furthermore, conventional approaches eliminate the passage of airflow, which is a requisite to myriad practical applications of noise attenuation [2,3].

Acoustic metamaterials (AMMs) represent an alternative paradigm by which to locally engineer effective material properties by precisely designing their constituent unit cells to manipulate acoustic wave propagation. As artificial structures, AMMs may introduce local resonances and exceptional acoustic properties, such as negative effective-mass density [4], negative effective-bulk modulus [5], or a combination of both [6,7]. With advances in AMMs, unprecedented approaches to manipulating acoustic waves have been reported, thereby realizing various applications, including acoustic cloaking [8–16], wave-front manipulation [17–19], and acoustic hologram [20–23], among others [6,7,24–28]. While acoustic metamaterial-based structures have been proposed to attenuate sound efficiently, acoustic silencers reported to date have suffered from either narrowband working frequencies or the inability to function in the low-frequency regimes [29–31]. To date, AMMs enabling broadband noise attenuation capable of functioning in the low-frequency regimes remain an unmet need.

Mie resonances have been successfully used to create resonances for electric and magnetic fields [32–34]. Recently, with the adaptation of this concept to acoustics, this mechanism has been reported to contribute to a broad range of applications, including spatial sound concentration [35], nonradiative sound transceiver [36], and sound silencing [15]. In addition, Helmholtz resonators have also commonly been utilized to attenuate noise [37]. It has been verified that the bandwidth of acoustic silencing can be extended by parallel arrangements of multiple Helmholtz resonators featuring different resonant frequencies [38]. In order to preserve the Helmholtz resonator array's broadband attenuation while enhancing resonant mode intensity at the low-frequency range, we propose a composite AMM composed of Mie resonators and a Helmholtz resonator array. Herein, we propose a composite AMM, which is realized by combining Mie resonators with a Helmholtz resonator array. The reported approach serves to yield efficient broadband sound attenuation, especially in the low-frequency regime. The acoustic attenuation performance of this design is theoretically, numerically, and experimentally demonstrated. Of note, the central open region provides ventilation in applications requiring airflow but may be generalized to allow for the passage of other background mediums. This design provides a pathway towards noise mitigation for various practical scenarios in which

*xinz@bu.edu
†stephan.anderson@bmc.org

 

broadband noise mitigation in low-frequency regimes in combination with sustained airflow is required.

## II. RESULTS AND DISCUSSION

### A. Properties of the composite acoustic metamaterial units

The schematic diagram of the composite acoustic metamaterial is shown in Fig. 1(a). The structure consists of six Mie resonators (SMR) and a Helmholtz resonator (HR) arrayed horizontally. In theory, Mie resonance is realized through the contrast in refractive indices between the resonance unit and the background medium. Therefore, instead of supporting only one monopolar resonance as is the case in other types of acoustic resonators, Mie resonators can exhibit multiple resonance modes [35]. Herein, the contrast in refractive index is achieved through the application of space-coiling metastructures, which can efficiently coil up space in order to delay the propagating acoustic wave phase to mimic a high refractive index [39]. The SMR unit cell in our design is a circular structure with an inner radius $r$ and outer radius $R$. The circumferential region of the SMR unit cell is divided into six branch channels, each of which consists of a space-coiling metastructure of channel width $w$ and a curling number $N = 8$. Given the high degree of impedance mismatch between the solid frame and the background medium (air), as scalar waves, acoustic waves propagate along the zigzag channel without a cutoff frequency. In the case of the SMR unit cell shown in Fig. 1(b), the wave path $L$ is depicted as the orange line, which is 7.57 times longer than a straight line from the channel inlet to the outlet $R - r$, which enables a high refractive index relative to air (mass density of air, $\rho_0 = 1.22$ kg/m$^3$; speed of sound in air, $c_0 = 343$ m/s). According to the effective medium theory, six effective mediums with larger refractive indices may be used to analyze the acoustic properties of the SMR; an effective physical model is then illustrated as the rightward figure in Fig. 1(b). Here, the effective refractive index is determined by the ratio of the elongated wave path to the direct distance between the inlet and outlet point. The speed of sound in the effective medium $c_e$ is given by Eq. (1). Additionally, by applying the impedance-matching condition, the effective-mass density of the effective medium $\rho_e$ can also be derived. The effective parameters of each effective medium channel can be extracted as follows [40]:

$$c_e = \frac{(R-r)c_0}{L}, \quad \rho_e = \frac{4\pi L \rho_0 R}{2Nw(R-r)}. \tag{1}$$

The HR array in the composite AMM consists of eight HR unit cells with differing geometries. In each unit, the neck and cavity represent the acoustic mass and capacitor of the mass-spring oscillator system, respectively. During the acoustic waves' propagation in the duct, the pressure variation in the neck area leads to oscillation of air in the neck region, radiating sound into the adjacent cavity. Thus, such local resonances create an equivalent negative bulk modulus to realize sound attenuation in a narrowband frequency regime. As shown in Fig. 1(c), in the HR array, those HR units are designed with resonant frequencies equally distributed within the frequency band ranging from 200 to 1000 Hz (Table I). The eight HR unit cells all share an identical cavity volume $V_c = 13\,289$ mm$^2$ and length of their necks $l_n = 5.75$ mm. The neck area for each unit and its corresponding resonant frequency $f_i$ are calculated [Eq. (2)] [41] and listed in Table I:

TABLE I. Geometrical parameters of HR units.

| Unit $i$ | 1 | 2 | 3 | 4 | 5 | 6 | 7 | 8 |
|---|---|---|---|---|---|---|---|---|
| $S_i$ (mm$^2$) | 1.4 | 3.15 | 5.1 | 7.97 | 11.48 | 20.41 | 31.89 | 45.92 |
| $f_i$ (Hz) | 216 | 314 | 389 | 473 | 552 | 700 | 836 | 963 |

$$f_i = \frac{c_0}{2\pi}\sqrt{\frac{S_i}{l_i V_c}}, \quad l_i = l_n + \gamma r_i, \tag{2}$$

where $l_i$ is the effective length of the tube, $\gamma$ is the end correction factor, and $r_i$ is the radius of neck.

### B. Theory of the composite acoustic metamaterial

In order to predict the acoustic performance of the composite AMM design, the transfer-matrix method and the lumped-element model are applied to analyze the SMR unit cell and the HR array separately. Generally, a transfer matrix $T_0$ is used to relate the acoustic pressure and particle velocity at the front ($x = 0$) and rear ($x = d$) surface of a given structure as follows:

$$\begin{bmatrix} P \\ V \end{bmatrix}_{x=0} = T_0 \begin{bmatrix} P \\ V \end{bmatrix}_{x=d}, \tag{3}$$

where $P$ is the acoustic pressure and $V$ is the normalized acoustic particle velocity. In the case of the SMR unit cell, the acoustic performance is attributed to both the area-changing duct and the effective mediums of the six space-coiling components. Therefore, the transfer matrix $T_0$ for the SMR unit cell in duct is rewritten as $T_0 = T_f T_s T_r$, in which $T_s$ refers to the transfer matrix for the SMR unit cell, $T_f$ ($T_r$) refers to the contribution of the front (rear) area-changing duct, which is given by [42]

$$T_f\ (T_r) = \begin{bmatrix} \cos(k_0 L_c) & j\sin(k_0 L_c)/\phi_0 \\ j\phi_0 \sin(k_0 L_c) & \cos(k_0 L_c) \end{bmatrix}, \tag{4}$$

where $k_0$ is the wave number of acoustic waves in air, $L_c = 0.5H + 0.95R(1 - 1.25\sqrt{\phi_0})$ is the effective length of the front (rear) area-changing duct [43], $H$ is the thickness of the SMR unit cell, and $\phi_0$ is the area-changing ratio

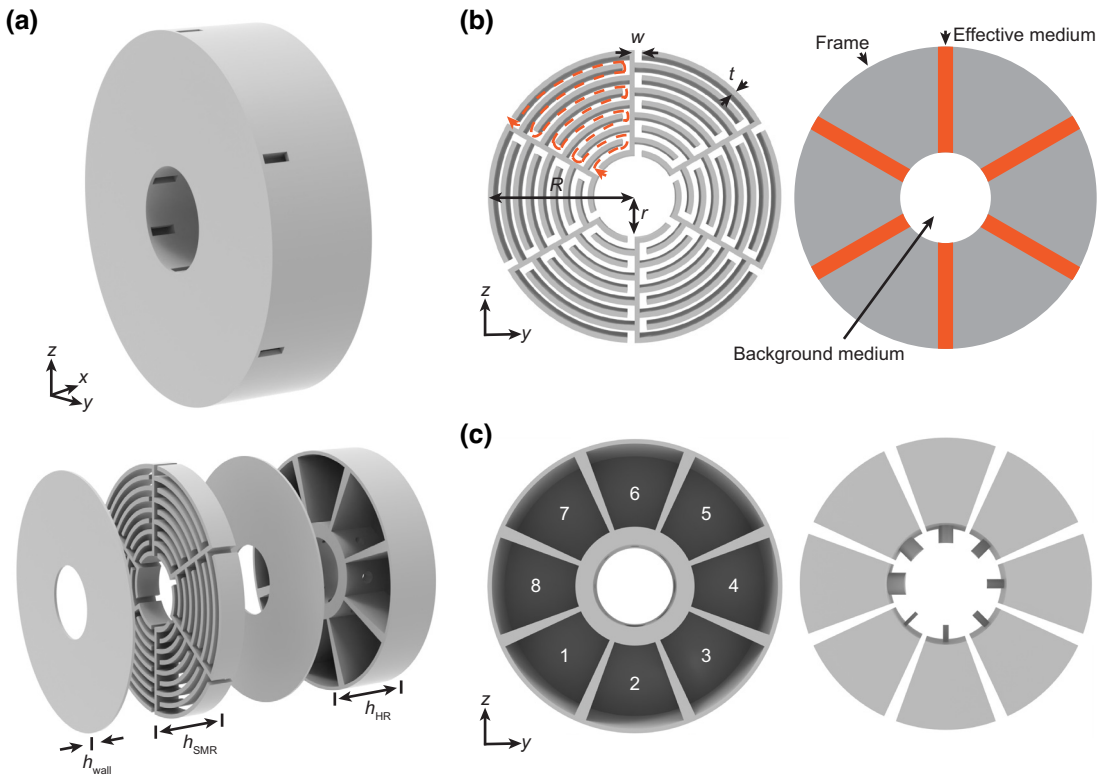


FIG. 1. (a) Schematic diagram of the composite acoustic metamaterial and its components. The thickness of the internal walls $h_{\text{wall}} = 1$ mm, the thickness of the SMR unit cell $h_{\text{SMR}} = 10$ mm, and the thickness of the HR array $h_{\text{HR}} = 20$ mm. (b) Cross-section view of an SMR unit cell with outer radius $R = 50$ mm. The circumferential region is divided into six side-branch space-coiling metastructure units with the following geometric parameters: the width of the space-coiling channels $w = 0.05R$, the thickness of the structure frame $t = 0.035R$, and the curling number $N = 8$. The radius of the inner open area $r = R - (N + 1) \times t - N \times w$. The wave path $L$ is depicted as the orange line. The equivalent model of an SMR unit cell is shown as the rightward figure. (c) The Helmholtz resonator array is composited of eight Helmholtz resonator unit cells, which all share an identical cavity volume and neck length but differ in their neck areas.

of the duct ($\phi_0 = r^2/R^2$). Since all six effective mediums share the same $x$-axis location and are in parallel with one another, they can be recognized as six discrete lumped elements. The acoustic effective impedance of each effective medium is represented as $Z_e = -j\,\rho_e c_e \cot(k_e L_e)/\xi\rho_0 c_0$, where $k_e$ is the wave number of acoustic waves in the effective medium, $L_e$ is the length of the effective medium, and $\xi$ is the ratio of the cross-section area of the effective medium to its opening area [44,45]. The total acoustic impedance for one SMR unit cell is represented as $Z_s = [(h/2H) \times (6/Z_e)]^{-1}$ and the transfer matrix for the SMR unit cell is

$$T_s = \begin{bmatrix} 1 & 0 \\ \frac{6S_e}{S_d Z_s} & 1 \end{bmatrix}, \tag{5}$$

where $h$ is the thickness of the effective medium, $S_e$ is the open area of each effective medium, and $S_d$ is the cross-section area of the area-changing duct. Therefore, the transmission loss (TL) through one SMR unit cell may be derived as

$$TL = 20\log_{10}\left(\left|\frac{1}{2}\left(T_{11} + T_{12} + T_{21} + T_{22}\right)\right|\right), \tag{6}$$

where $T_{i,j}\,(i,j = 1,2)$ corresponds to the element in $T_0$. The theoretical prediction of transmission loss as a function of frequency is plotted as the red line with square markers in Fig. 2(a). To validate the theoretical analysis, the SMR unit cell is numerically simulated by using the "Pressure acoustics, frequency domain" of COMSOL Multiphysics. In the simulation, a frequency sweep is conducted and the TL of the SMR unit is plotted as the red line in Fig. 2(a), noting that the simulated result agrees well with the theoretical derivation. Owing to the high-intensity Mie resonance at the first two modes (330 and 986 Hz), the TL of the SMR unit cell increases significantly, reaching 14 and 45 dB, respectively. The acoustic pressure fields inside the SMR unit cell at these two frequencies are also simulated and plotted as the inset figures in Fig. 2(a). The axially symmetrical patterns confirm the

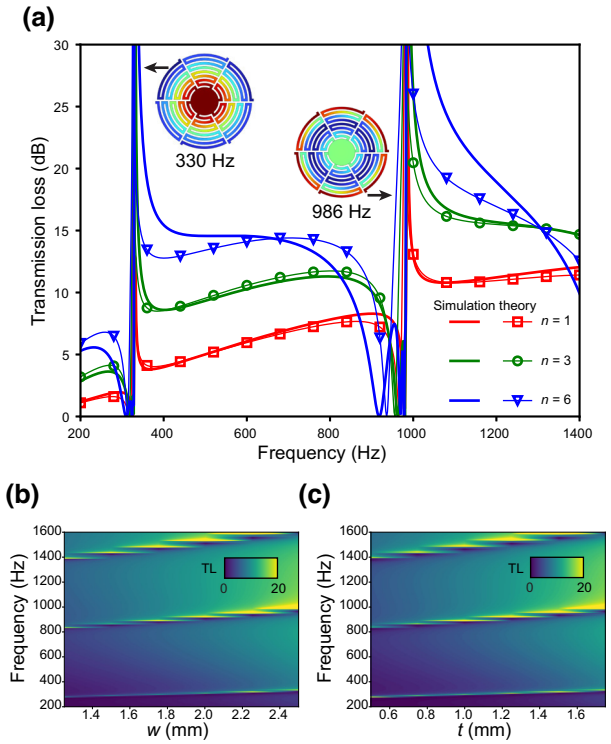


FIG. 2. (a) Theoretical (lines with markers) and simulated (lines) TL as a function of frequency for the SMR unit with different unit numbers $n = 1, 3, 6$ along the $x$ direction. Inserted figures are the acoustic pressure distribution of SMR unit at the resonant frequencies. (b) Simulated TL with $n = 3$ as functions of the frequency and the channel width $w$. (c) Simulated TL with $n = 3$ as functions of the frequency and the frame thickness $t$.

existence of monopolar Mie resonance inside the SMR unit. Additionally, since the space-coiling metastructure lies perpendicular to the $x$ axis, the thickness of the SMR unit is on a deep subwavelength scale. Through stacking SMR units, an improved acoustic attenuation effect may be realized. To demonstrate this possibility, numerical and theoretical analyses are conducted on the structure as a function of increasing the number of SMR units. As shown in Fig. 2(a), when $n$ increases to 3 (green lines) and 6 (blue lines), the acoustic attenuation bandwidth decreases slightly, but the amplitude increases substantially. Save for the slight TL amplitude shift resulting from the co-resonances between unit cells when $n = 6$, a high degree of agreement is demonstrated between the theory and simulated results.

To yield a more comprehensive understanding of the effects of geometric parameters on the SMR's acoustic performance, parameter sweeps are conducted to determine the TL in different configurations of the SMR unit cell. Here, the number of SMR unit cells is chosen as $n = 3$. The results of TL as functions of the frequency, the width of the space-coiling channels $w$, and the thickness of the structure frame $t$ are plotted in Figs. 2(b) and 2(c). When $w$ and $t$ increase, the total length of the wave path $L$ as well as the openness decrease, and the Mie resonances move toward higher frequencies.

As for the HR array, the acoustic impedance of each HR unit cell depends on its branch tube and cavity, which represent a lumped inertance and a lumped compliance, respectively. The acoustic impedance at the interface of one HR unit cell is given by [41]

$$Z_i = j\,\rho_0 \left(\omega \frac{l_i}{S_i} - \frac{c_0^2}{\omega V_c}\right) + \frac{\omega^2 \rho_0}{\pi c_0}, \tag{7}$$

where $\omega$ is the angular frequency in rad/s. As the eight HR unit cells are assembled parallel to each other, the acoustic impedance of the HR array is given by

$$Z_h = \left(\sum \frac{r_i}{2H}\left(\frac{1}{Z_i}\right)\right)^{-1} \quad (i = 1 \ldots 8). \tag{8}$$

Then, the transfer matrix is expressed by

$$T_h = \begin{bmatrix} 1 & 0 \\ \frac{\rho_0 c_0}{S_d Z_h} & 1 \end{bmatrix}. \tag{9}$$

Similarly, the TL of the HR array layer is calculated numerically and analytically, as presented in Fig. 3(a). It is seen that the soundproofing effects appear at eight frequencies, corresponding to the resonance modes of the eight HR units. At each peak, the designated HR unit resonates and creates a localized acoustic pressure field, which leads to a sound blocking effect at a narrow bandwidth frequency region. Figure 3(b) shows the acoustic pressure distributions inside the HR array at different resonant modes (modes 1–8). The $i_{\text{th}} (i = 1, 2, \ldots, 8)$ HR unit is "active" to block sound at corresponding frequencies and leads to a peak in the transmission loss spectrum.

Finally, the SMR unit cell is connected with an HR array to achieve high performance, wideband, low-frequency acoustic attenuation. To achieve a satisfactory silencing effect at low frequency while maintaining a deep subwavelength structure, we select the number of SMR units to be $n = 3$. Numerical simulation is initially performed to derive the transmission loss of the composite design, and the transfer matrix for the composite structure in duct may be derived by $T_t = T_f T_s T_h T_r$. The theoretically derived transmission loss is then calculated based on the derived transfer matrix $T_t$ and Eq. (6), as shown as the dashed line with square markers in Fig. 4. The calculated results show good agreement with the simulated data.

### C. Experimental validation

To experimentally verify the soundproofing effect, the impedance tube and two-load method are employed to test the acoustic attenuation of the proposed design. Figure 5(a)

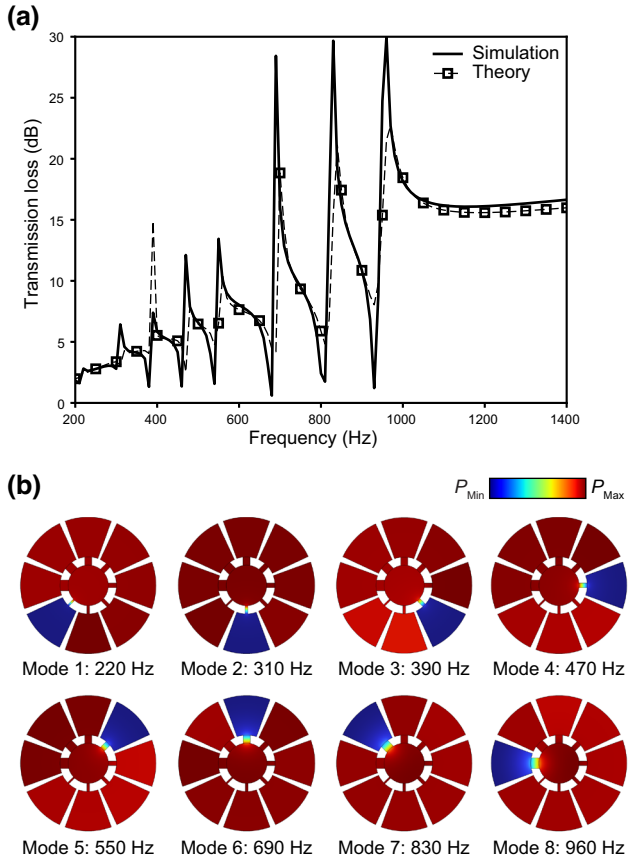


FIG. 3. (a) Theoretical (lines with markers) and simulated (lines) TL as a function of frequency for the HR array. (b) Cross-section view of acoustic pressure distribution of the HR array at different resonant frequencies (TL peaks) in (a).

is the schematic diagram of the impedance tube setup. The fabricated, composite AMM sample is mounted snugly in the sample holder and four microphones are placed in

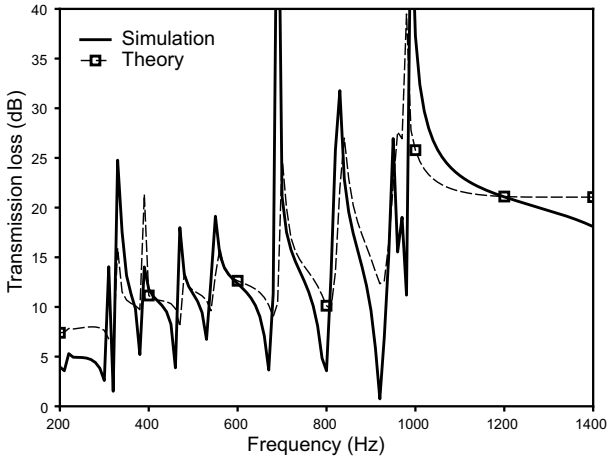


FIG. 4. Theoretical (dashed line) and simulated (solid line) TL as a function of frequency for the composite AMM (three SMR units with one HR array).

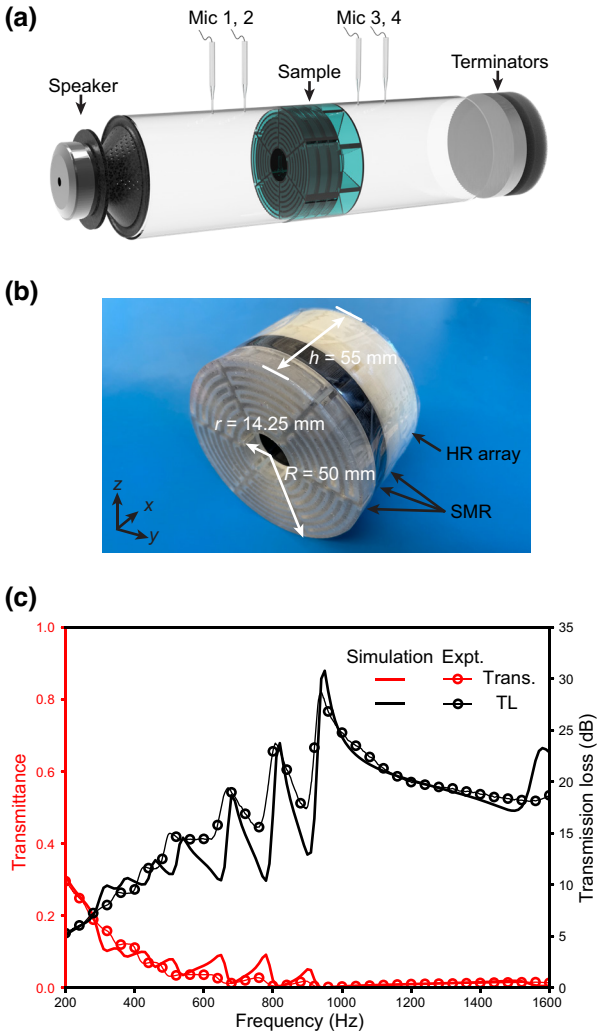


FIG. 5. (a) Schematic diagram of impedance tube setup. (b) The fabricated sample is printed with SLA and FDM three-dimensional printing technologies in sizes $r = 14.25$ mm, $R = 50$ mm, and $h = 55$ mm. (c) Simulated and measured transmittance and transmission loss of the composite AMMs when $n = 3$.

the front and rear positions of the impedance tube. Then, the transfer matrix and two-load method are conducted to measure the transmission loss and the transmission coefficient of the sample. To ease the difficulty of fabrication, SMR unit cells and the HR array component of the composite AMM are printed separately with the former printed via stereolithography (SLA) and the latter printed through fused deposition modeling (FDM). The finalized composite AMM is then assembled by gluing together all components, as shown in Fig. 5(b). Notably, the fabricated sample is 55 mm in thickness and can be considered as a deep subwavelength structure compared to the wavelength at the operational center frequency (428 mm in 800 Hz). The measured transmittance and transmission loss are shown by the red and black lines with markers

in Fig. 5(c), respectively. For comparison, a numerical simulation is conducted on the composite AMM. As the branch channels in the SMR and the neck areas of the HR array are very small compared to the wavelength, the dissipation of acoustic energy due to the thermal viscosity should be considered. Therefore, the "Thermalviscous acoustics, frequency domain" module in COMSOL Multiphysics is applied to small regions of the composite AMM. The similarity between the simulated and measured results confirms the broadband acoustic attenuation effect (up to 28-dB transmission loss) within the range of 350 to 1600 Hz, yielding an acoustic power transmission lower than 10% within a bandwidth of 1250 Hz. The peaks in transmission loss spectra correspond to the composite resonance modes due to the monopolar Mie resonances and HR units' resonances. Specifically, this design provides high-performance sound attenuation in the low-frequency regime, and this attenuation effect can be further increased by stacking additional SMR units, albeit with atrade-off between structure thickness and silencing performance. Moreover, this design maintains a constant area, which supports steady ventilation.

## III. CONCLUSION

In summary, we theoretically and experimentally demonstrate the acoustic attenuation effect of a composite acoustic metamaterial consisting of a Mie resonator and a Helmholtz resonator array. The transfer-matrix method and the lumped-element model are applied to predict the acoustic behavior of the components theoretically. The experimentally measured result shows good agreement with simulation. Through the composite design, using a deep-subwavelength structure, we successfully achieve a broadband low-frequency acoustic attenuation that blocks over 90% of incident acoustic energy within a frequency range of 1250 Hz. The relatively thin dimensions of the SMR unit cell offer the possibility of further strengthening the attenuation in the low-frequency regime by stacking additional unit cells within the metamaterial. This work establishes the underpinnings of a class of structures enabling the realization of high-performance noise attenuation in the low-frequency regime, while maintaining airflow, the practical applications of which are broad and diverse.

## ACKNOWLEDGMENT

The author would like to thank Boston University Photonics Center for funding and technical support.

## APPENDIX A: THE EFFECTIVENESS OF COMPOSITE DESIGN

In order to verify the effectiveness of the composite design, two simulations are conducted, both of which consider thermal viscosity. As shown in Fig. 6, the composite design is firstly compared with six SMR units in terms of transmission loss. At low frequencies, both structures demonstrate comparable acoustic attenuation performance. However, as the frequency increases, the composite design outperforms the six SMR units due to the inclusion of the HR array. Then, the transmission-loss comparison of the composite design with three HR arrays is depicted in Fig. 7. The composite design provides improved acoustic attenuation at frequencies below 500 Hz due to the inclusion of SMR units. Furthermore, the composite design is also approximately 10 mm thinner than the three Helmholtz resonator arrays. Additionally, two supplementary experiments are carried out to verify the enhanced resonance intensity in the low-frequency region (<500 Hz) achieved by introducing additional SMR units.

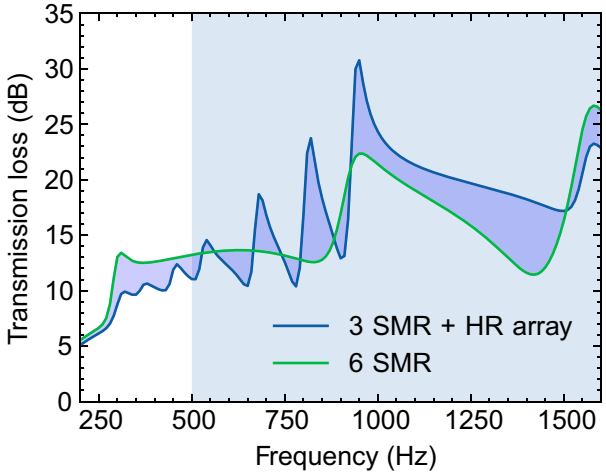


FIG. 6. Simulated transmission loss of three SMR units with one HR array compared with six SMR units alone.

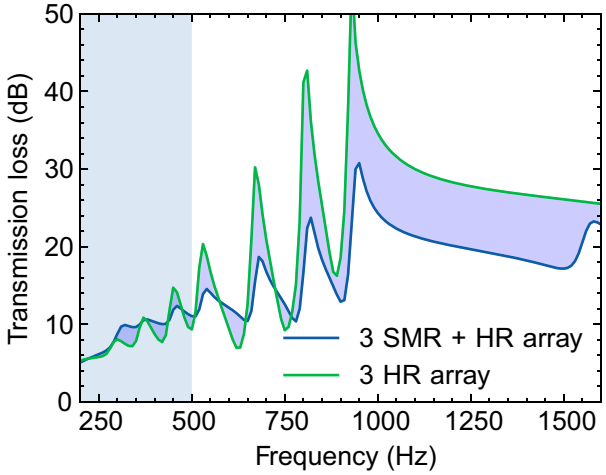


FIG. 7. Simulated transmission loss of three SMR units with one HR array compared with three HR arrays alone.

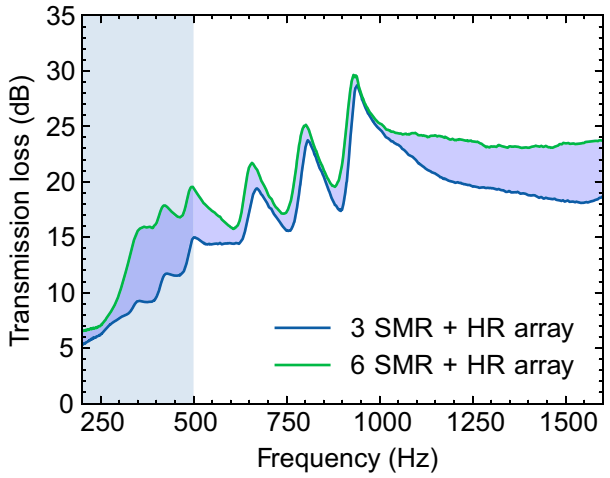


FIG. 8. Measured transmission loss of three SMR units with one HR array and six SMR units with one HR array.

Figure 8 demonstrates the comparison of an HR array combined with three and six SMR units. By inserting three additional SMR units, it is evident that the acoustic insulation at the low-frequency range (<500 Hz) has been significantly improved, aligning with the first resonance mode of the SMR unit.

To conclude, the composite design outperforms the homogeneous design in terms of broad bandwidth and high transmission loss at the low-frequency region. The performance at the low-frequency region can be further improved by inserting additional SMR units, with a penalty of an increasingly bulky structure being imposed.

## APPENDIX B: REFLECTION AND ABSORPTION

At the low-frequency range, the viscous loss cannot be ignored, as the viscous boundary layer's thickness is comparable to the channel's size. To further explore the underlying working mechanism of the composite design, an experiment is conducted to determine the absorption and reflection behavior of the structure, as shown in Fig. 9.

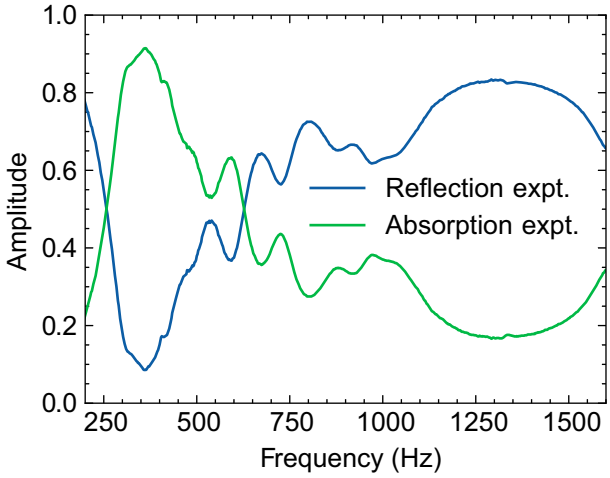


FIG. 9. Measured absorption and reflection of the composite AMM.

The results reveal that the wide band acoustic attenuation is achieved via the synergy of reflection and absorption. Here, the absorption is calculated by $\alpha = 1 - |R^2|$. At 346 Hz, the highest peak of absorption indicates a strong energy absorption provided by the first resonance mode of the SMR units. At other frequencies, the structure functions through the synergy of absorption and reflection.

[1] J. Mei, G. Ma, M. Yang, Z. Yang, W. Wen, and P. Sheng, Dark acoustic metamaterials as super absorbers for low-frequency sound, Nat. Commun. **3**, 1 (2012).
[2] H. Slabbekoorn, Noise pollution, Curr. Biol. **29**, R957 (2019).
[3] Y. Kajikawa, W.-S. Gan, and S. M. Kuo, Recent advances on active noise control: Open issues and innovative applications, APSIPA Trans. Signal Inf. Process. **1**, e3 (2012).
[4] Z. Yang, J. Mei, M. Yang, N. Chan, and P. Sheng, Membrane-Type Acoustic Metamaterial with Negative Dynamic Mass, Phys. Rev. Lett. **101**, 204301 (2008).
[5] N. Fang, D. Xi, J. Xu, M. Ambati, W. Srituravanich, C. Sun, and X. Zhang, Ultrasonic metamaterials with negative modulus, Nat. Mater. **5**, 452 (2006).
[6] J. Li and C. T. Chan, Double-negative acoustic metamaterial, Phys. Rev. E **70**, 055602 (2004).
[7] S. H. Lee, C. M. Park, Y. M. Seo, Z. G. Wang, and C. K. Kim, Composite Acoustic Medium with Simultaneously Negative Density and Modulus, Phys. Rev. Lett. **104**, 054301 (2010).
[8] S. A. Cummer, B.-I. Popa, D. Schurig, D. R. Smith, J. Pendry, M. Rahm, and A. Starr, Scattering Theory Derivation of a 3D Acoustic Cloaking Shell, Phys. Rev. Lett. **100**, 024301 (2008).
[9] J. Li and J. B. Pendry, Hiding Under the Carpet: A New Strategy for Cloaking, Phys. Rev. Lett. **101**, 203901 (2008).
[10] M. Farhat, S. Guenneau, and S. Enoch, Ultrabroadband Elastic Cloaking in Thin Plates, Phys. Rev. Lett. **103**, 024301 (2009).
[11] B.-I. Popa, L. Zigoneanu, and S. A. Cummer, Experimental Acoustic Ground Cloak in Air, Phys. Rev. Lett. **106**, 253901 (2011).
[12] S. Zhang, C. Xia, and N. Fang, Broadband Acoustic Cloak for Ultrasound Waves, Phys. Rev. Lett. **106**, 024301 (2011).
[13] M. D. Guild, M. R. Haberman, and A. Alù, Plasmonic-type acoustic cloak made of a bilaminate shell, Phys. Rev. B **86**, 104302 (2012).
[14] N. Stenger, M. Wilhelm, and M. Wegener, Experiments on Elastic Cloaking in Thin Plates, Phys. Rev. Lett. **108**, 014301 (2012).
[15] L. Sanchis, V. M. García-Chocano, R. Llopis-Pontiveros, A. Climente, J. Martínez-Pastor, F. Cervera, and J. Sánchez-Dehesa, Three-Dimensional Axisymmetric Cloak Based on the Cancellation of Acoustic Scattering from a Sphere, Phys. Rev. Lett. **110**, 124301 (2013).

[16] D. L. Sounas, R. Fleury, and A. Alù, Unidirectional Cloaking Based on Metasurfaces with Balanced Loss and Gain, Phys. Rev. Appl. **4**, 014005 (2015).
[17] Y. Xie, W. Wang, H. Chen, A. Konneker, B.-I. Popa, and S. A. Cummer, Wavefront modulation and subwavelength diffractive acoustics with an acoustic metasurface, Nat. Commun. **5**, 1 (2014).
[18] Y. Li, X. Jiang, R.-q. Li, B. Liang, X.-y. Zou, L.-l. Yin, and J.-c. Cheng, Experimental Realization of Full Control of Reflected Waves with Subwavelength Acoustic Metasurfaces, Phys. Rev. Appl. **2**, 064002 (2014).
[19] G. Ma, M. Yang, S. Xiao, Z. Yang, and P. Sheng, Acoustic metasurface with hybrid resonances, Nat. Mater. **13**, 873 (2014).
[20] K. Melde, A. G. Mark, T. Qiu, and P. Fischer, Holograms for acoustics, Nature **537**, 518 (2016).
[21] A. Marzo, S. A. Seah, B. W. Drinkwater, D. R. Sahoo, B. Long, and S. Subramanian, Holographic acoustic elements for manipulation of levitated objects, Nat. Commun. **6**, 8661 (2015).
[22] Y. Zhu, J. Hu, X. Fan, J. Yang, B. Liang, X. Zhu, and J. Cheng, Fine manipulation of sound via lossy metamaterials with independent and arbitrary reflection amplitude and phase, Nat. Commun. **9**, 1632 (2018).
[23] Y. Xie, C. Shen, W. Wang, J. Li, D. Suo, B.-I. Popa, Y. Jing, and S. A. Cummer, Acoustic holographic rendering with two-dimensional metamaterial-based passive phased array, Sci. Rep. **6**, 35437 (2016).
[24] Z. Liu, X. Zhang, Y. Mao, Y. Zhu, Z. Yang, C. T. Chan, and P. Sheng, Locally resonant sonic materials, Science **289**, 1734 (2000).
[25] C. Goffaux, J. Sánchez-Dehesa, A. L. Yeyati, P. Lambin, A. Khelif, J. Vasseur, and B. Djafari-Rouhani, Evidence of Fano-Like Interference Phenomena in Locally Resonant Materials, Phys. Rev. Lett. **88**, 225502 (2002).
[26] J. Lydon, M. Serra-Garcia, and C. Daraio, Local to Extended Transitions of Resonant Defect Modes, Phys. Rev. Lett. **113**, 185503 (2014).
[27] T. Brunet, A. Merlin, B. Mascaro, K. Zimny, J. Leng, O. Poncelet, C. Aristégui, and O. Mondain-Monval, Soft 3D acoustic metamaterial with negative index, Nat. Mater. **14**, 384 (2015).
[28] L. Shen, Y. Zhu, F. Mao, S. Gao, Z. Su, Z. Luo, H. Zhang, and B. Assouar, Broadband Low-Frequency Acoustic Metamuffler, Phys. Rev. Appl. **16**, 064057 (2021).
[29] R. Ghaffarivardavagh, J. Nikolajczyk, S. Anderson, and X. Zhang, Ultra-open acoustic metamaterial silencer based on Fano-like interference, Phys. Rev. B **99**, 024302 (2019).
[30] C. Liu, J. Shi, W. Zhao, X. Zhou, C. Ma, R. Peng, M. Wang, Z. H. Hang, X. Liu, and J. Christensen, *et al.*, Three-Dimensional Soundproof Acoustic Metacage, Phys. Rev. Lett. **127**, 084301 (2021).
[31] A. Chen, X. Zhao, Z. Yang, S. Anderson, and X. Zhang, Broadband Labyrinthine Acoustic Insulator, Phys. Rev. Appl. **18**, 064057 (2022).
[32] Q. Zhao, J. Zhou, F. Zhang, and D. Lippens, Mie resonance-based dielectric metamaterials, Mater. Today **12**, 60 (2009).
[33] L. Kang and D. Lippens, Mie resonance based left-handed metamaterial in the visible frequency range, Phys. Rev. B **83**, 195125 (2011).
[34] L. Shi, T. U. Tuzer, R. Fenollosa, and F. Meseguer, A new dielectric metamaterial building block with a strong magnetic response in the sub-1.5-micrometer region: Silicon colloid nanocavities, Adv. Mater. **24**, 5934 (2012).
[35] Y. Cheng, C. Zhou, B. Yuan, D. Wu, Q. Wei, and X. Liu, Ultra-sparse metasurface for high reflection of low-frequency sound based on artificial Mie resonances, Nat. Mater. **14**, 1013 (2015).
[36] J. Zhang, W. Rui, C. Ma, Y. Cheng, X. Liu, and J. Christensen, Remote whispering metamaterial for non-radiative transceiving of ultra-weak sound, Nat. Commun. **12**, 1 (2021).
[37] S.-H. Seo and Y.-H. Kim, Silencer design by using array resonators for low-frequency band noise reduction, J. Acoust. Soc. Am. **118**, 2332 (2005).
[38] H. Nguyen, Q. Wu, X. Xu, H. Chen, S. Tracy, and G. Huang, Broadband acoustic silencer with ventilation based on slit-type Helmholtz resonators, Appl. Phys. Lett. **117**, 134103 (2020).
[39] Z. Liang and J. Li, Extreme Acoustic Metamaterial by Coiling Up Space, Phys. Rev. Lett. **108**, 114301 (2012).
[40] J. Zhao, L. Zhang, and Y. Wu, Enhancing monochromatic multipole emission by a subwavelength enclosure of degenerate Mie resonances, J. Acoust. Soc. Am. **142**, EL24 (2017).
[41] M. Munjal, *Acoustics of Ducts and Mufflers* (Wiley, Chichester, 2014).
[42] U. Ingard, On the theory and design of acoustic resonators, J. Acoust. Soc. Am. **25**, 1037 (1953).
[43] S. Huang, X. Fang, X. Wang, B. Assouar, Q. Cheng, and Y. Li, Acoustic perfect absorbers via spiral metasurfaces with embedded apertures, Appl. Phys. Lett. **113**, 233501 (2018).
[44] S. Huang, Z. Zhou, D. Li, T. Liu, X. Wang, J. Zhu, and Y. Li, Compact broadband acoustic sink with coherently coupled weak resonances, Sci. Bull. **65**, 373 (2020).
[45] R. Dong, D. Mao, X. Wang, and Y. Li, Ultrabroadband Acoustic Ventilation Barriers via Hybrid-Functional Metasurfaces, Phys. Rev. Appl. **15**, 024044 (2021).